

Sparsity-regularized coded ptychography for robust and efficient lensless microscopy on a chip

Ninghe Liu^{1,2}, Qianhao Zhao², Guoan Zheng^{2*}

¹Weiyang College, Tsinghua University, Beijing 100084, China

²Department of Biomedical Engineering, University of Connecticut, Storrs, CT 06269, USA

*Correspondence: G. Z. (guoan.zheng@uconn.edu)

Abstract: In ptychographic imaging, the trade-off between the number of acquisitions and the resultant imaging quality presents a complex optimization problem. Increasing the number of acquisitions typically yields reconstructions with higher spatial resolution and finer details. Conversely, a reduction in measurement frequency often compromises the quality of the reconstructed images, manifesting as increased noise and coarser details. To address this challenge, we employ sparsity priors to reformulate the ptychographic reconstruction task as a total variation regularized optimization problem. We introduce a new computational framework, termed the ptychographic proximal total-variation (PPTV) solver, designed to integrate into existing ptychography settings without necessitating hardware modifications. Through comprehensive numerical simulations, we validate that PPTV-driven coded ptychography is capable of producing highly accurate reconstructions with a minimal set of eight intensity measurements. Convergence analysis further substantiates the robustness, stability, and computational feasibility of the proposed PPTV algorithm. Experimental results obtained from optical setups unequivocally demonstrate that the PPTV algorithm facilitates high-throughput, high-resolution imaging while significantly reducing the measurement burden. These findings indicate that the PPTV algorithm has the potential to substantially mitigate the resource-intensive requirements traditionally associated with high-quality ptychographic imaging, thereby offering a pathway toward the development of more compact and efficient ptychographic microscopy systems.

Keywords: Ptychography, compressive sensing, proximal algorithm, coherent diffraction imaging, lensless microscopy, phase retrieval.

Introduction

The phase of light plays a crucial role in optical imaging, determining the propagation of it whether in free space or during its interaction with a sample. However, detectors are limited to capturing solely the intensity, making phase retrieval a formidable and ill-posed challenge. To address this fundamental limitation, ptychography emerged as a powerful technique, initially designed for electron crystallography¹ but subsequently adapted for optical applications. Ptychography operates by acquiring a multitude of diverse diffraction patterns while a coherent probe beam systematically scans the specimen. This strategic collection of measurements with inherent redundancy resulting from overlapping illuminated regions, significantly enhances the successful retrieval of both phase and amplitude information. Modern ptychography systems have evolved to incorporate iterative phase retrieval frameworks, applying constraints in both real and reciprocal space to iteratively refine estimates^{2,3}. Rooted in its foundation of multi-measurement configurations and iterative phase retrieval algorithms, ptychography has developed rapidly and diversified into various forms and applications⁴⁻¹⁶.

Multiple overlapping areas of illumination is essential for the success of ptychographic reconstruction. In the traditional situation of single-measure phase retrieval, there could be multiple potential objects, each with varying amplitude and phase, that can yield identical intensity patterns at the sensor plane. By harnessing multiple measurements, ptychography effectively mitigates these inherent ambiguities. This is achieved by imposing diverse probe beams on the same objects, specifically within the overlapping regions, thereby substantially enhancing the prospects of a successful recovery. However, the pursuit of a reconstruction that combines high accuracy and resolution demands the acquisition of numerous measurements, often numbering in the hundreds or even thousands. Consequently, this approach necessitates a time-consuming and equipment-intensive process, engendering a trade-off between measurement quantity and the resultant image quality.

To address this challenge and fully unlock the information contained within a limited set of measurements, we draw inspiration from the principles of compressive phase retrieval techniques^{17, 18}, which hold the promise of pushing the boundaries of phase recovery beyond the conventional information-theoretic limit by exploring signal priors to a greater extent. Notably, within the domains of single-shot phase retrieval and holography, sparsity priors in various domains including spatial¹⁹⁻²¹, gradient²²⁻²⁸, wavelet²⁹ and other forms^{30, 31} have proven to be effective regularizers, providing theoretical foundation for the introduction of sparsity into wide-field, high-resolution ptychographic reconstruction.

In this paper, we center on the gradient-domain sparsity to innovate ptychographic reconstruction. The ptychographic reconstruction problem is remodeled through the formulation of an objective function that combines a fidelity term, which signifies the disparity between the recovered wave field and the intensity measurements, with an additional total variation (TV)-regularization term. On account of the piece-wise smoothness property of TV model and its computationally efficient algorithms^{28, 32, 33}, our proposed ptychographic reconstruction model not only enables the representation of multidimensional features, including three-dimensional phase variation but also guarantees its generalizability to various sample scenarios. We introduce a ptychographic proximal TV-solver (PPTV) and seamlessly implement this optimization framework into our unique coded ptychography system without any hardware modifications. Both numerical simulations and experimental results have demonstrated that the PPTV-driven coded ptychography approach substantially reduces the requisite number of intensity measurements while maintaining exceptionally satisfactory results. Our development of the PPTV algorithm represents as a significant contribution in alleviating the trade-off between high-quality ptychographic imaging and the resource-intensive demand of numerous measurements, thereby enhancing the feasibility of more compact and efficient ptychographic microscopy applications.

Methods

Preliminary illustrations on notations and forward model. In the following sections, the notations are defined as follows: The symbol $|\cdot|_p$, $(\cdot)^T$, $(\cdot)^*$, and $(\cdot)^H$ denotes the p -norm, transpose, conjugate and conjugate transpose (Hermitian) operators, respectively. \odot is the element-wise (Hadamard) multiplication operator for vectors, while $|\cdot|$, $|\cdot|^2$, $\sqrt{\cdot}$, and \cdot/\cdot should also be interpreted as element-wise operators when applied to vectors. $\text{diag}(\cdot)$ puts the entries of a vector into the diagonal of a matrix. For the convenience of illustration, we follow the convention of linear algebra and vectorize the two-dimensional wavefield as a one-dimensional vector representation. It is important to notice that vectorization is just for simplifying the notation and is not required for computation in practice.

In the forward model, the object O is first propagated by distance d_1 to the coded surface (CS) plane, where it is modulated by the spatially shifted coded sensor. On account of the relativity of displacement, the exit wave Ψ_{cs}^k downstream the object for the k -th scan position can be expressed as:

$$\Psi_{cs}^k = (H_k P_{d_1} O) \odot \phi_{cs} \quad (1)$$

where P_{d_1} and ϕ_{cs} represent the free space propagation for distance d_1 and the complex transmittance matrix of the CS, respectively. H_k stands for the spatial translation operation with respect to the k -th scan position. For the displacement (x_k, y_k) caused by the k -th translation, noticing that translation in spatial domain is equivalent to phase shift in Fourier domain, H_k can be written as:

$$H_k = \mathcal{F}^{-1} \{ e^{j2\pi(f_x x_k + f_y y_k)} \odot \mathcal{F} \} \quad (2)$$

\mathcal{F} and \mathcal{F}^{-1} denote the counterpart of 2D Fourier transform and inverse 2D Fourier transform in the expression of vectorized matrix and f_x and f_y are the corresponding frequency after Fourier transform operation. We denote $\Psi_u = P_{d_1} O$ and $\Psi_{us}^k = H_k \Psi_u$ for the convenience of following illustration. The exit wave Ψ_{cs}^k is then propagated to the sensor plane, where it is downsampled by image sensor pixels and recorded as intensity patterns. The intensity measurements y_i with respect to the k -th scan position can be expressed as:

$$y_k = S |P_{d_2} \Psi_{cs}^k|^2 \quad (3)$$

where P_{d_2} and S denote the free space propagation for distance d_2 and the downsampling matrix of the image sensor, respectively. Following the downsampling model in [11], Eq. (3) can be rewritten as:

$$y_k = B |P_{d_2} \Psi_{cs}^k|^2 + b \quad (4)$$

where B is a diagonally-dominant positive-definite matrix and b is a positive offset vector. For the simplest case we consider B as a discretized 0-1 matrix that fully collects all the energy on its pixels and b equals zero because for our system depicted in Fig 1(a), the whole image sensor is covered by the diffused laser.

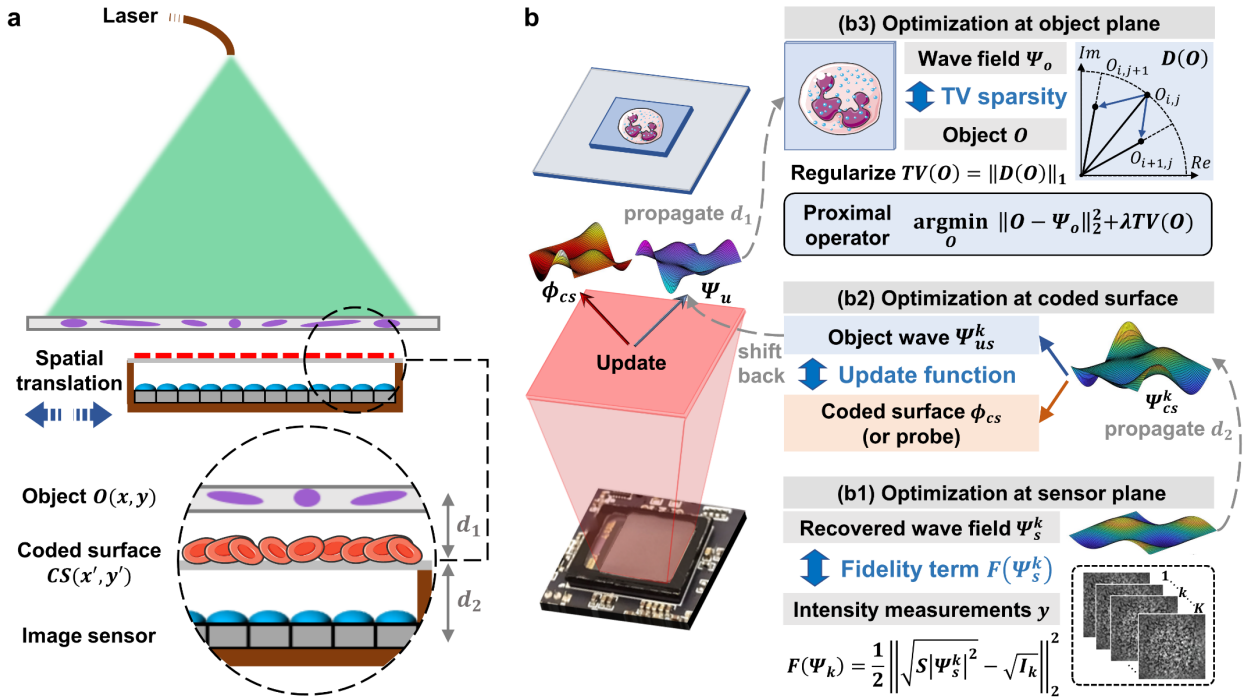


Figure 1. Coded ptychography system setup and the generalized reconstruction framework of PPTV. (a) Schematic of the reported device, where a blood-coated sensor is placed under the samples and translates across for multi-images acquisition. (b) Generalized ptychographic reconstruction framework, which outlines the key steps of PPTV

reconstruction. For conventional ptychography cases, the coded surface could be replaced by a probe. Generally, the reconstruction process proceeds through three steps: optimization at sensor plane for fidelity term, optimization at coded surface with the update function, and optimization at object plane with image sparsity prior. In this framework, the intensity measurements serve as posterior information, and when combined with proper sparsity prior, such as the TV regularization in our PPTV algorithm, the required number of intensity measurements can be substantially reduced.

Generalized reconstruction framework for ptychography. Based on the coded ptychography system depicted in Fig 1(a), We formulate the ptychography reconstruction as a constrained optimization problem, which can also generalize to other conventional ptychography cases where the coded surface should be replaced by a probe. Generally, the reconstruction process of PPTV can be divided into three subtasks, as is shown in Fig 1(b).

Step 1. Optimization at sensor plane. Search for the optimal wave field Ψ_k^{opt} that minimizes the distance between the intensity measurements I_k and the wave field intensity $|\Psi_s^k|^2$ given by the forward model, as is shown in Fig 1(b1).

$$(\Psi_s^k)^{opt} = \operatorname{argmin} d(I_k, |\Psi_s^k|^2) \quad (5)$$

$$d(I_k, |\Psi_s^k|^2) = F(\Psi_s^k) = \frac{1}{2} \left\| \sqrt{S|\Psi_s^k|^2} - \sqrt{I_k} \right\|_2^2 \quad (6)$$

In our work we choose the amplitude-based fidelity term as the distance metric because of its mathematical similarity to the Poisson noise model^{11,34}, which is proven to be an accurate model for noise statistics description. The detailed proof substantiating this choice is provided in the Supporting Information, Section 1. To optimize the fidelity term, we employ the gradient descent method, actively seeking to determine the optimal step size. The Wirtinger gradient is given by:

$$\nabla F(\Psi_s^k) = \frac{1}{2} \operatorname{diag}(\Psi_s^k) S^T \left(1 - \frac{\sqrt{I_k}}{\sqrt{S|\Psi_s^k|^2}} \right) \quad (7)$$

Once the locally optimal update direction is derived, we can perform the gradient descent operation:

$$(\Psi_s^k)' = \Psi_s^k - \beta_k \nabla F(\Psi_s^k) \quad (8)$$

where β_k is the step size for the descent direction. Notice that for specific update direction, the fidelity term can be seen as a convex function with respect to β_k , hence the optimal step size can be calculated by finding the extreme of $F(\beta_k)$:

$$\partial F(\beta_k) / \partial \beta_k = 0 \quad (9)$$

Solving Eq. (8) yields $\beta_k = 2$, thus we derive the optimal wave field for k -th scan position to be

$$(\Psi_s^k)^{opt} = \Psi_s^k \odot S^T \left(\frac{\sqrt{I_k}}{\sqrt{S|\Psi_s^k|^2}} \right) \quad (10)$$

which is equivalent to the well-known modulus constraint projection method.²

Step 2. Optimization at the coded surface. Apply a proper update function to the recovered wave field Ψ_{cs} at the coded surface plane, as is shown in Fig 1(b2). The uniqueness about ptychography is that the complex transmission matrix of the coded surface (or probe) is not accurately known, so a proper update

needs to be conducted on the back-propagated wave field at the coded surface plane Ψ_{cs}^k in order to recover the correct coded surface ϕ_{cs} and object-related wavefield Ψ_u . An error metric is introduced to evaluate the update process³⁵:

$$E = \|\Psi_{cs}^k - (H_k \Psi_u) \odot \phi_{cs}\|_2^2 \quad (11)$$

where $\Psi_{cs}^k = P_{d_2}^H(\Psi_s^k)^{opt}$. Again we calculate the Wirtinger gradient with respect to Ψ_u and ϕ_{cs} and take the gradient descent method to optimize E :

$$\nabla E_\Psi(\Psi_u) = H_k^H \left((\phi_{cs})^* \odot (\Psi_{us}^k \odot \phi_{cs} - \Psi_{cs}^k) \right) \quad (12)$$

$$\nabla E_\phi(\phi_{cs}) = (\Psi_{us}^k)^* \odot (\Psi_{us}^k \odot \phi_{cs} - \Psi_{cs}^k) \quad (13)$$

$$\Psi_u' = \Psi_u - \beta_u^k \nabla E_\Psi(\Psi_u) \quad (14)$$

$$\phi_{cs}' = \phi_{cs} - \beta_{cs}^k \nabla E_\phi(\phi_{cs}) \quad (15)$$

where $\Psi_{us}^k = H_k \Psi_u$ denotes the shifted object wave. [35] mentions that setting $\beta_u^k = \alpha_1 / |\phi_{cs}|_{max}^2$ and $\beta_{cs}^k = \alpha_2 / |\Psi_{us}^k|_{max}^2$ gives the classic ePIE update function for object and probe update⁴, while [11] takes another approach by neglecting second order terms and solving the step size with least-square (LSQ) method. After careful examination and calculation, we make a slight modification to the equation brought up in [11] and give the resulting LSQ matrix:

$$\begin{aligned} & \begin{pmatrix} \|\Delta\Psi_{us}^k \odot \phi_{cs}\|_2^2 + \alpha & Re\{(\Delta\Psi_{us}^k \odot \phi_{cs})^H(\Delta\phi_{cs} \odot \Psi_{us}^k)\} \\ Re\{(\Delta\Psi_{us}^k \odot \phi_{cs})^H(\Delta\phi_{cs} \odot \Psi_{us}^k)\} & \|\Delta\phi_{cs} \odot \Psi_{us}^k\|_2^2 + \alpha \end{pmatrix} \begin{pmatrix} \beta_u^k \\ \beta_{cs}^k \end{pmatrix} \\ & = \begin{pmatrix} Re\{(\Delta\Psi_{us}^k \odot \phi_{cs})^H \mathcal{X}\} \\ Re\{(\Delta\phi_{cs} \odot \Psi_{us}^k)^H \mathcal{X}\} \end{pmatrix} \quad \beta_u^k, \beta_{cs}^k \in \mathbb{R} \end{aligned} \quad (16)$$

where $\mathcal{X} = \Psi_{cs}^k - \Psi_{us}^k \odot \phi_{cs}$ represents the residual term and α is a small regularization term to prevent numerical instability. $\Delta\Psi_{us}^k = -H_k \nabla E_\Psi(\Psi_u^k)$ and $\Delta\phi_{cs} = -\nabla E_\phi(\phi_{cs})$ are the update direction for shifted object wave and coded surface. Re denotes the real part of a complex number, and \mathbb{R} is the real number constraint that step size ought to satisfy. Derivation of this is also provided in our Supporting Information, Section 2. In PPTV we simply choose the parameters that lead to ePIE update function in consideration of computational cost, while comparison between PPTV and this LSQ-ML method is also given in the following illustration.

Step 3. Optimization at object plane. Use prior information to further optimize the recovered wave field at the object plane, as is shown in Fig 1(b3). So far, all information for the recovery process has been derived from the intensity measurements, often requiring a substantial number of measurements if no additional knowledge is available. However, in PPTV, we transcend the limitations of relying solely on posterior information and incorporate TV regularization into our imaging model. This advancement allows us to minimize the total variation of an image, equating to enhanced gradient sparsity—a universally applicable prior for natural images. The generalizability of PPTV is further validated through a series of numerical simulations and optical experiments with different biological samples.

We consider the discrete anisotropic complex TV semi-norm depicted in Fig 1(b3):

$TV(O) = \|D(O)\|_1 = \sum_{i=1}^{N_1-1} \sum_{j=1}^{N_2} |O_{i+1,j}^m - O_{i,j}^m| + \sum_{i=1}^{N_1} \sum_{j=1}^{N_2-1} |O_{i,j+1}^m - O_{i,j}^m|$ (17) where $O^m \in \mathbb{C}^{N_1 \times N_2}$ with $n = N_1 \times N_2$ denotes the non-vectorized two-dimensional image. Operator D computes the spatial finite difference for the vectorized object O along both directions. Given the back propagated wave field Ψ_o , the third step optimization can be formulated as a proximal operator:

$$prox_v = \operatorname{argmin}_O \frac{1}{2} \|O - \Psi_o\|_2^2 + \lambda TV(O) \quad (18)$$

The purpose of this operator is to minimize the TV term while maintaining the proximity of our final solution to Ψ_o , which is derived from preceding two optimization steps. The parameter λ can serve as a regularization factor to control the permissible deviation from Ψ_o . This operator coincides with solving the TV-regularized image denoising problem^{28, 32, 33, 36, 37}, and the optimal solution O^{opt} can be solved via the dual problem:

$$\min_{w \in S} \left\{ G(w) \equiv \|\Psi_o - D^H w\|_2^2 \right\} \quad (19)$$

$$W = \{w_i \mid \|w_i\|_\infty \leq \lambda\} \quad (20)$$

$$O^{opt} = \Psi_o - D^H w^{opt} \quad (21)$$

where $w \in \mathbb{C}^{2n}$ denotes the dual variable, which is confined to convex set W , the final solution for object O^{opt} can be represented by the optimal solution for the dual variable w^{opt} . Proof of this is given in our Supporting Information, Section 3. Although Eq. (18) looks like a least square problem, it cannot be directly solved because the complex finite difference operator D cannot be represented explicitly in a matrix form, hence the pseudo-inverse of DD^H could not be derived. Alternatively, we use the accelerated gradient projection algorithm to solve this problem in a more computation-effective way. By calculating the Wirtinger gradient of $G(w)$, we iteratively perform gradient descent and project the updated solution onto set W using the projection operator $P_w(\cdot)$. The step size η for this gradient descent update is set as $1/8$ based on the convergence analysis presented in Supporting Information, Section 3.

$$\nabla_w G(w) = -D(\Psi_o - D^H w) \quad (22)$$

Chart 1. Solver for TV-regularized subproblem

Input: wave field Ψ_o , step size η , $\varepsilon_t = t/(t + 3)$, and subiteration number T

1. $w^{(0)} = 0, z^{(0)} = w^{(0)}$
 2. **For** $t = 1, 2, \dots, T$ **do**
 3. $w^{(t)} = P_w \left(z^{(t-1)} - \eta \nabla_z G(z^{(t-1)}) \right)$ Gradient projection
 4. $z^{(t)} = w^{(t)} + \varepsilon_t (w^{(t)} - w^{(t-1)})$ Nesterov's extrapolation
 5. **End for**
 6. $O^{opt} = \Psi_o - D^H w^{opt}$
-

Objective modeling and the PPTV algorithm. After step-by-step derivation of PPTV algorithm, we present a unified objective modeling that integrate all three subtasks optimization, which can be expressed as:

$$\min_{O, CS} \sum_k \frac{1}{2K} \|A_{CS}^k O - \sqrt{I_k}\|_2^2 + R(O) \quad (23)$$

where A_{CS}^k is the discussed forward model with respect to the coded surface ϕ_{CS} and the k -th scan position (x_k, y_k) , I_k is the corresponding measurement intensity, and R is the regularization term that represents sparsity prior. Optimization at the sensor plane and the coded surface corresponds to minimizing the first fidelity term, and optimization at the object plane corresponds to minimizing the second regularization term, which equals to $\lambda TV(O)$ in our case. We furthermore improve the algorithm's robustness and convergence speed by mini-batch optimization and Nesterov's extrapolation, and give the PPTV algorithm, as is shown in Fig. 2.

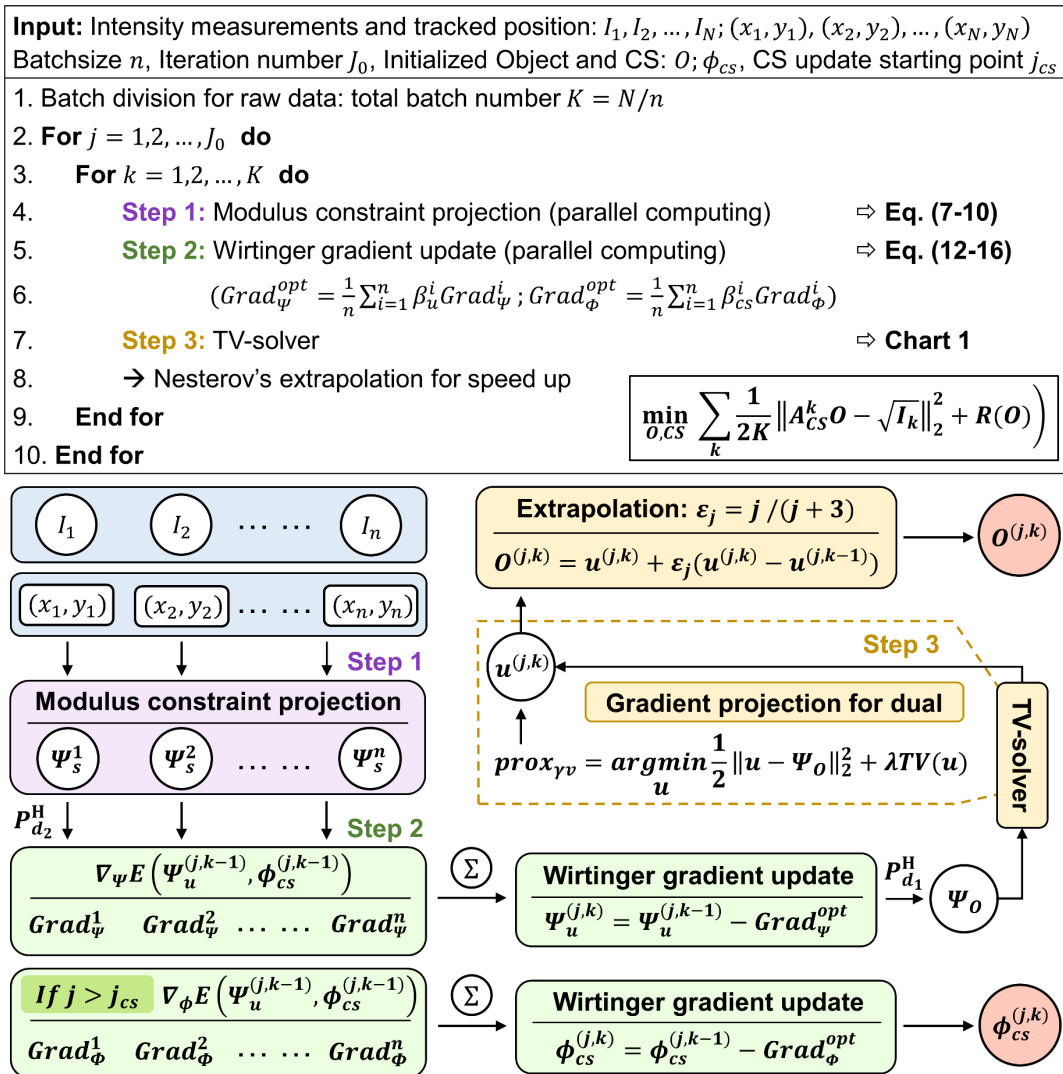


Figure 2. Algorithm workflow of PPTV reconstruction. The three steps of optimization are integrated into an iterative optimization framework. In the practical operation of PPTV, step 1 and step 2 are performed in parallel computing. Commonly, coded surface is not updated from the very beginning, so in this workflow we denote the update starting point as j_{CS} .

Results

Numerical simulations and analysis. The advantages of the presented method are demonstrated on realistic numerical simulations because it allows us to avoid potential errors in sample positions, and instability of illumination. Also, in numerical simulation reconstruction quality can be completely evaluated and analyzed in a quantitative way. Firstly, we assume the complex transmittance matrix of the coded surface is already known and generate the coded surface as a randomly initialized complex matrix. We compare the reconstructions of ePIE, LSQ-ML method, and PPTV in numerical simulations, as is shown in Fig. 3.

The ground truth for ptychographic reconstruction is a complex wave field whose amplitude is the “street” image and phase the “peppers” image, as are shown in Fig. (a1) and Fig. (a2). A homogeneous intensity of 0.2 was added to simulate the background. In this ideal case, the coded surface is not updated, which corresponds to $j_{CS} > J_0$ in the workflow in Fig. 2. The amplitude and phase map of it are shown in Fig. (b1) and Fig. (b2). In order to test the performance of PPTV in case of low measurement number, we only take 8 measurements corresponding to different spatial translation locations shown in Fig. (3c). The original image size is 1024×1024 , while the sensor resolution is set to be 256×256 , which means the super-resolution (SR) ratio equals 4 in our case. The iteration number is chosen so that total runtime cost of the three methods are close to each other while convergence is also guaranteed. The relative root mean square error (RMSE) is calculated between the reconstructions and the ground truth to quantitatively represent the reconstruction quality. From the results given in Fig. (d1-d3), we can see that in similar amount of time, the reconstruction of PPTV has the highest accuracy in overall as well as in detail: The RMSE error is reduced by an order of magnitude compared to the other two methods, and the zoomed-in amplitude and phase show excellent noise-free details.

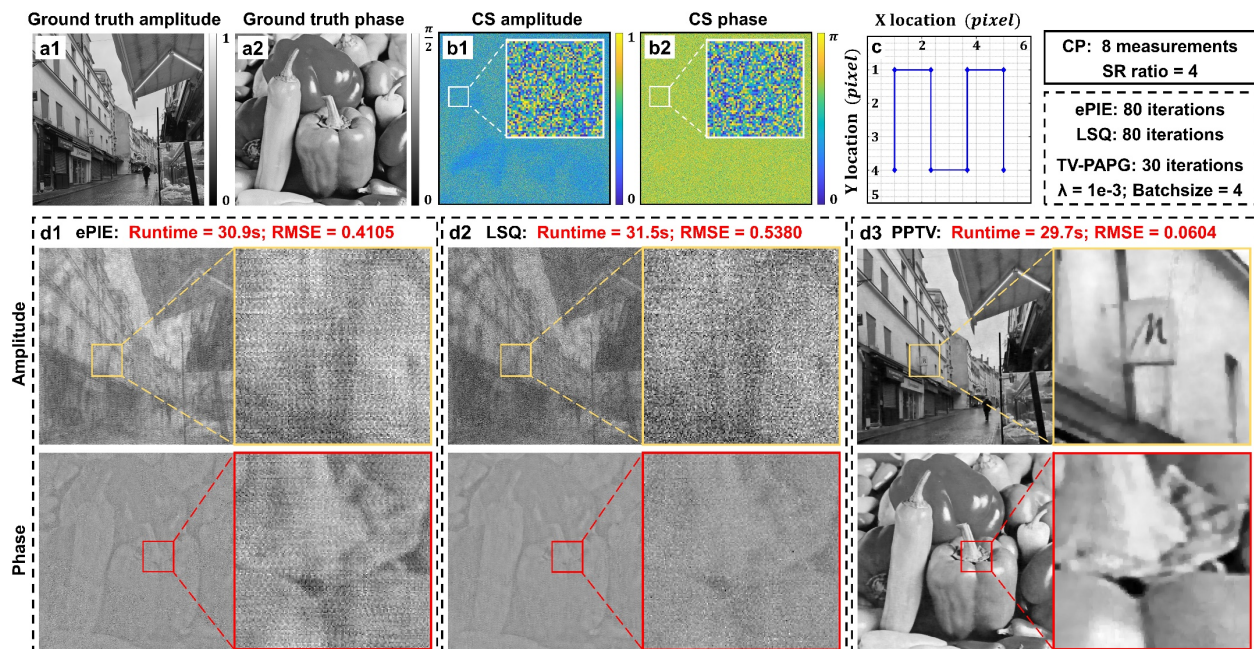


Figure 3. Simulation parameters setup and comparison of numerical reconstructions among ePIE, LSQ-ML, and PPTV. (a1-a2) Ground truth amplitude and phase of object. (b1-b2) Amplitude and phase of simulated coded surface. (c) Simulated translation positions. (d1-d3) Reconstructions of object with ePIE, LSQ-ML, and PPTV methods.

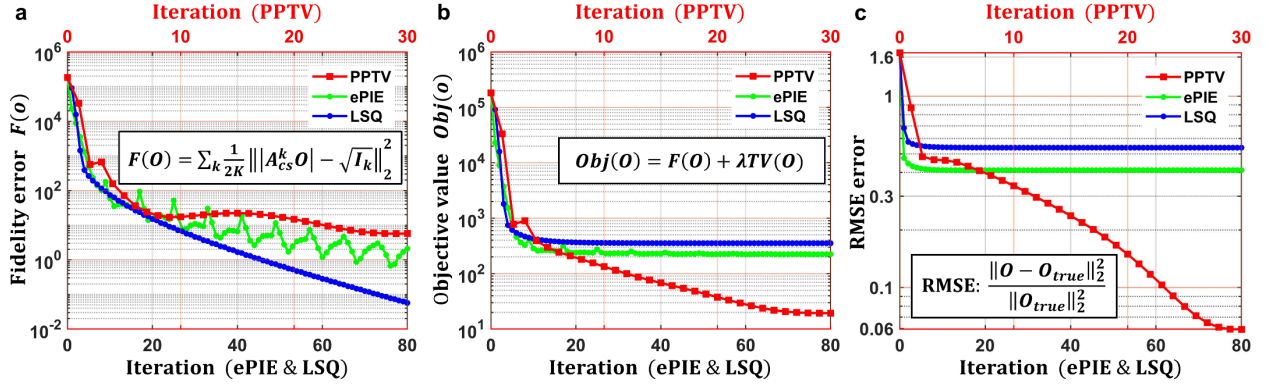


Figure 4. Convergence analysis of ePIE, LSQ-ML, and PPTV for 8-measurements numerical simulations. (a) Fidelity error against iterations for different reconstruction algorithms. (b) Objective value against iterations for different reconstruction algorithms. (c) RMSE error against iterations for different reconstruction algorithms.

In order to verify the effectiveness of the objective modeling in Eq. (23), we further analyze the convergence behavior of ePIE, LSQ-ML, and PPTV against iterations for 8-measurements numerical simulations, as is shown in Fig. (4). Specifically, we choose the fidelity error in Eq. (6) that represents the similarity between diffraction patterns and intensity measurements at the sensor plane, the objective function in Eq. (23) that embodies the essence of PPTV method, and the RMSE error that can be seen as a golden standard for reconstruction quality evaluation. For ePIE and LSQ-ML method, the fidelity error reaches a rather low value and continues to decrease with each iteration in Fig. (4a). However, the objective value has already converged and remains static after approximately 20 iterations in Fig. (4b), a trend mirrored by RMSE in Fig. (4c). In contrast, the PPTV approach exhibits a higher fidelity error compared to ePIE and LSQ-ML. Nevertheless, both the objective value and RMSE error for PPTV continue to decrease significantly, ultimately reaching a much lower level than the other two methods. This observation emphasizes the superior characterization of the reconstruction process by the PPTV objective modeling, which goes far beyond the fidelity error. Additionally, it is worth noting that the LSQ-ML method achieves a fidelity error lower than ePIE, yet its RMSE error is higher. This discrepancy can be attributed to the inherent ambiguities that arise when working with fewer intensity measurements, highlighting the limitations of relying solely on the fidelity error for modeling the reconstruction process and emphasizing the necessity of introducing sparsity priors, as exemplified by our PPTV approach.

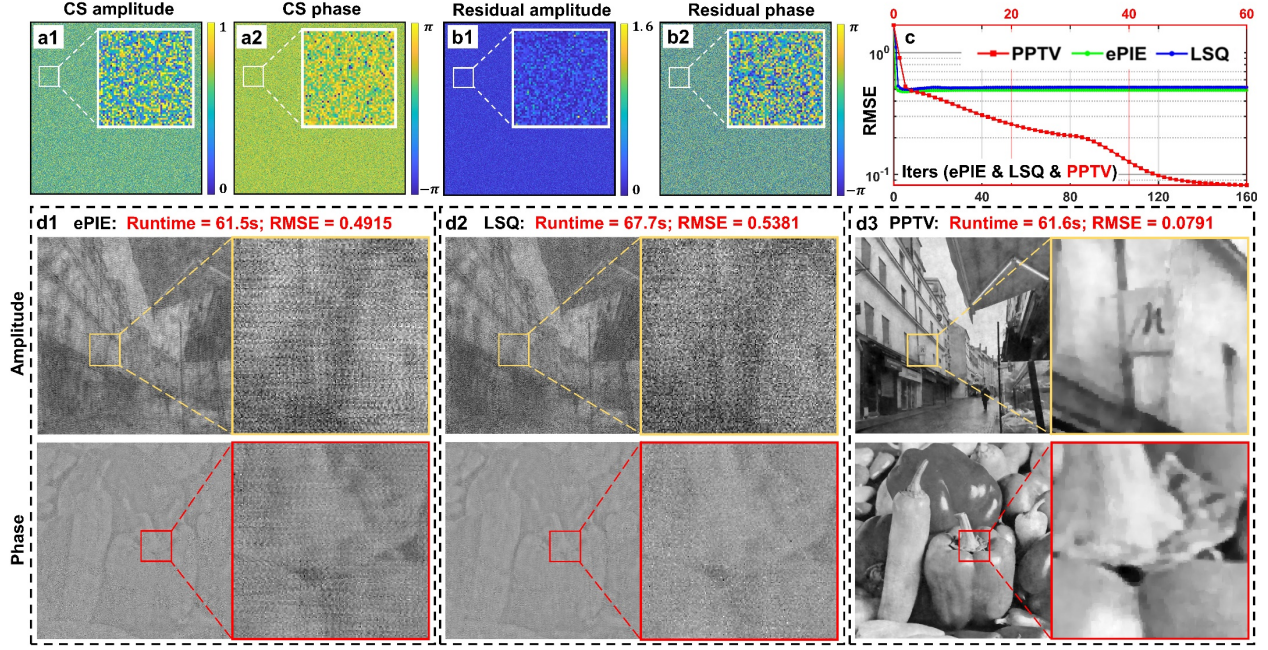


Figure 5. Coded surface initialization, convergence curve and comparison of numerical reconstructions among ePIE, LSQ-ML, and PPTV. (a1-a2) Amplitude and phase map of the initialized coded surface. (b1-b2) Amplitude and phase map of the complex residuals between the initialization and the ground truth coded surface. (c) RMSE convergence curve with respect to the three reconstruction methods. (d1-d3) Reconstructions of object with ePIE, LSQ-ML, and PPTV methods.

In the practical application of coded ptychography and conventional ptychography, the complex transmittance matrix of coded surface (or probe) is not accurately known. To simulate this common situation, we add a rather high level of Gaussian noise to the amplitude and phase of the coded surface for initialization and perform a bi-directional reconstruction on both object and coded surface.

$$\phi_{CS}^{ini} = \mathcal{P}_I \left((|\phi_{CS}| + \mathcal{N}(0, \sigma_{amp})) \exp(j(\text{angle}(\phi_{CS}) + \sigma_{ang})) \right) \quad (24)$$

$$I = \{\phi_i \mid \|\phi_i\|_{\infty} \leq 1\} \quad (25)$$

where $\mathcal{N}(\mu, \sigma)$ is the normal distribution with mean and variance to be μ and σ , $\text{angle}(\cdot)$ takes the angle of a complex vector, and $\mathcal{P}_I(\cdot)$ denotes the projection operator onto the constraint I and guarantees the modulus of ϕ_{CS}^{ini} does not exceed one. Amplitude and phase map of the disturbed coded surface are shown in Fig. 5(a1) and Fig. 5(a2). The amplitude and phase map of the complex residuals between the initialization and the ground truth coded surface are shown in Fig. 5(b1) and Fig. 5(b2). Besides the iterations performed in the former cases, we take another same number of iterations for bi-directional update, which corresponds to $j_{CS} = J_0/2$ in the workflow in Fig. 2. Reconstruction results of the three methods are compared in Fig. 5(d1-d3), and RMSE convergence curve is given in Fig. 5(c). Although the RMSE of PPTV reconstruction is slightly higher than the ideal case, the image quality still far exceeds ePIE and LSQ-ML reconstructions, with detailed information fully recovered, such as the letter “M” in the amplitude map and the stalk of peppers in the phase map. Furthermore, the RMSE convergence curve of PPTV exhibits a clear turn point at iteration 30. This inflection signifies that the updates applied to the object and coded surface continue to lead the reconstruction in the right direction, indicating ongoing improvement. In contrast, for ePIE and LSQ-ML methods, no apparent enhancements are evident after the initiation of coded

surface updates, which demonstrates the effectiveness of PPTV in guiding the bi-directional reconstruction of both object and coded surface. We further analyze the influence of regularization parameter λ in PPTV's reconstruction, and verify that choosing $\lambda = 1 \times 10^{-3}$ achieves the best performance in our numerical setup, which is provided in the Supporting Information, Section 4.

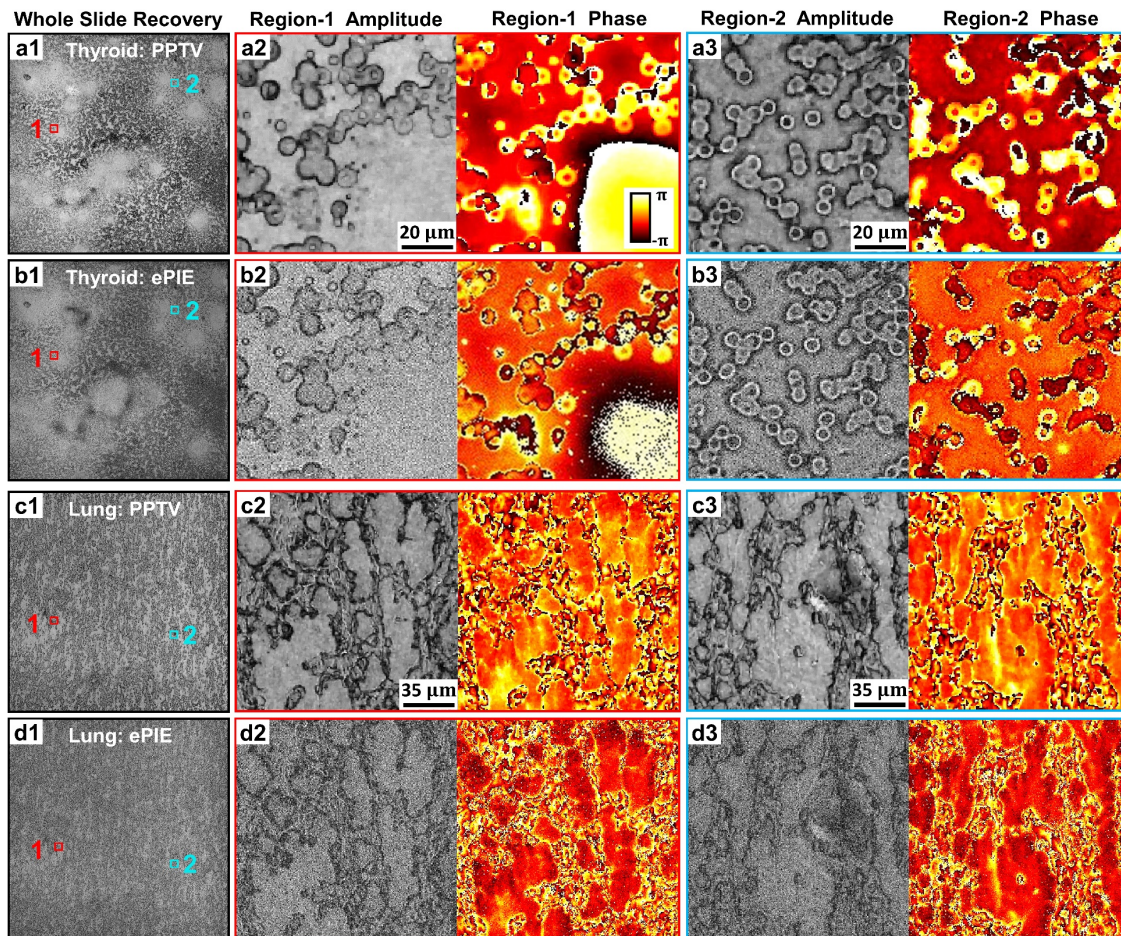


Figure 6. Whole slide imaging for biological samples. Comparisons between PPTV (a) and ePIE (b) reconstructions of unstained thyroid smear sample. Comparisons between PPTV (c) and ePIE (d) reconstructions of the unstained lung smear sample.

Experiments for biological samples imaging. In Fig. 6, we show the whole slide recovery results of different thyroid smear samples using only 50 intensity measurements, which is merely a fraction of the original measurements with data reduced by a factor of ten. Given our previous analysis of the similarity between the LSQ-ML method and ePIE besides adjustment solely in step size, and the implications of such adjustments on reconstruction quality with a limited number of measurements, we chose ePIE as the basis for comparison in our reconstruction evaluations. Specifically, in Fig. 6(a) and Fig. 6(b), PPTV reconstruction of the unstained thyroid sample clearly outperforms ePIE, presenting a noise-free imaging and reveals the inside structure of the surrounding blood cells in Fig. 6(a2). Fig. 6(c) also shows the PPTV reconstruction of amplitude and phase of the unstained thyroid smear sample, while its counterpart of ePIE in Fig. 6(d) suffers from noise disturbance and loss of crucial details.

The strengths of PPTV are further demonstrated when addressing challenging scenarios characterized by pathological changes and increased tissue thickness, circumstances in which traditional reconstruction methods like ePIE struggle to produce satisfactory results. To illustrate this scenario, we select another

unstained thyroid smear sample and take 300 measurements for the reconstruction process, a larger dataset necessitated by the challenges posed by this sample. Specifically, as depicted in Figure 7(a), we zoomed in on Region-1, where lesions are present. In this region, ePIE-based recovery fails to distinguish cell boundaries adequately. On the contrary, PPTV excels in recovering these tissues, presenting the line trace with better smoothness, as is shown in Fig. 7(b). In Region-2, representing the recovery of normal cells, PPTV once again shows its robust noise-reduction capabilities, further underscoring its effectiveness in challenging imaging scenarios.

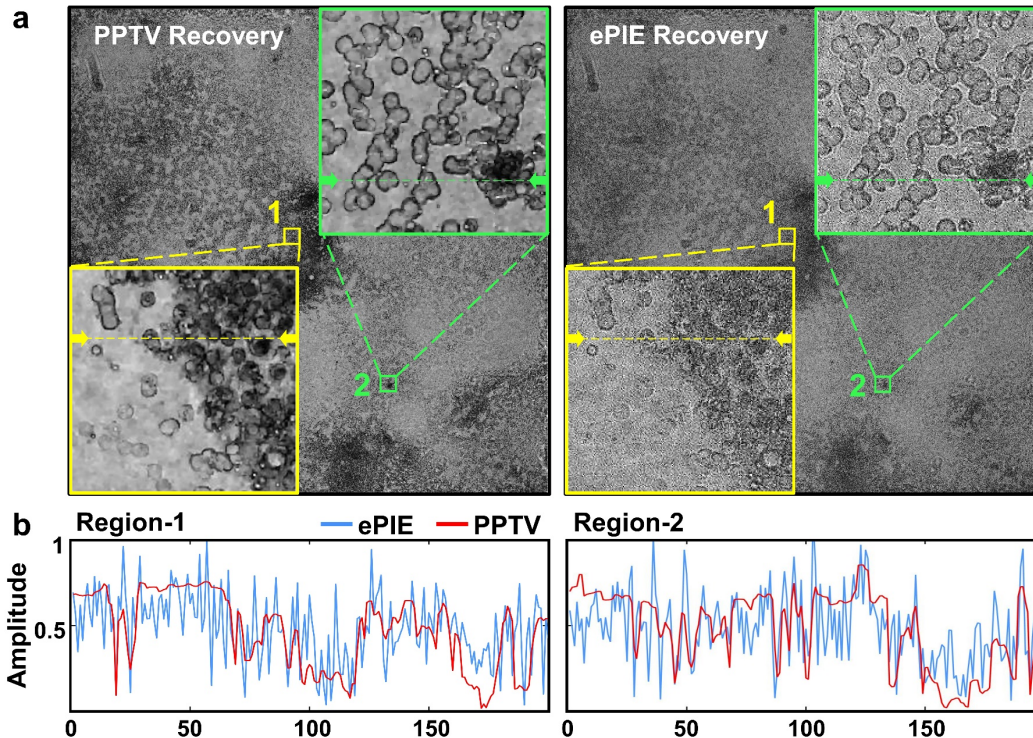


Figure 7. Whole slide imaging for a challenging unstained thyroid smear sample. (a) Comparisons between PPTV and ePIE reconstructions of thyroid smear sample. Region-1 is where the lesion occurs and region-2 represents recovery of normal cells. (b) Line traces of region-1 and region-2 zoomed-in recovery.

Discussion and conclusion

The trade-off between measurement quantity and the imaging quality presents a formidable challenge, hindering the widespread applications of ptychography for optical microscopy. Here, we develop the PPTV algorithm to achieve high-throughput, high-resolution ptychographic microscopy while substantially reducing the number of required intensity measurements. The contributions and innovations of the reported reconstruction algorithm can be summarized as follows. First, we introduce a novel objective modeling approach for ptychographic reconstruction problem. By incorporating sparsity regularization to the fidelity term, the intrinsic information of intensity measurements is fully unlocked, setting the stage for superior imaging with fewer measurements. Second, our theoretical analysis greatly contributes to hyperparameter selection in each optimization step, providing guidance for further manual tuning. Third, the proposed three-step optimization of PPTV establishes a generalized framework for various ptychographic systems and presents a practical way for implementing image priors into ptychography reconstruction through proximal algorithms.

While our work employs TV sparsity as the regularization term, it's worth noting that implicit priors derived from more advanced methods like BM3D and deep networks³⁸⁻⁴³ can also be seamlessly integrated into the third optimization step. It's important to acknowledge that while gradient sparsity proves to be a universal prior for natural images, the quest for more suitable and effective image priors remains an essential way for future research.

Acknowledgment

G.Z. acknowledges the support of National Institute of Health R01-EB034744, the UConn SPARK grant, and National Science Foundation 2012140. Q.Z. acknowledges the support of GE fellowship.

Author contributions

N.L. and G.Z. conceived the project. N.L. developed the prototype systems and prepared the display items. All authors contributed to the writing of the manuscript.

Competing interests

The authors declare no competing financial interest.

Reference:

- (1) Hoppe, W., Diffraction in inhomogeneous primary wave fields. 1. Principle of phase determination from electron diffraction interference. *Acta Crystallogr. A* **1969**, *25*, 495-501.
- (2) Fienup, J. R., Reconstruction of an object from the modulus of its Fourier transform. *Opt. Lett.* **1978**, *3* (1), 27-29.
- (3) Faulkner, H. M. L.; Rodenburg, J., Movable aperture lensless transmission microscopy: a novel phase retrieval algorithm. *Physical review letters* **2004**, *93* (2), 023903.
- (4) Maiden, A. M.; Rodenburg, J. M., An improved ptychographical phase retrieval algorithm for diffractive imaging. *Ultramicroscopy* **2009**, *109* (10), 1256-1262.
- (5) Dierolf, M.; Menzel, A.; Thibault, P.; Schneider, P.; Kewish, C. M.; Wepf, R.; Bunk, O.; Pfeiffer, F., Ptychographic X-ray computed tomography at the nanoscale. *Nature* **2010**, *467* (7314), 436-439.
- (6) Maiden, A. M.; Humphry, M. J.; Zhang, F.; Rodenburg, J. M., Superresolution imaging via ptychography. *J. Opt. Soc. Am. A* **2011**, *28* (4), 604-612.
- (7) Thibault, P.; Menzel, A., Reconstructing state mixtures from diffraction measurements. *Nature* **2013**, *494* (7435), 68-71.
- (8) Zheng, G.; Horstmeyer, R.; Yang, C., Wide-field, high-resolution Fourier ptychographic microscopy. *Nature Photonics* **2013**, *7* (9), 739-745.
- (9) Pfeiffer, F., X-ray ptychography. *Nature Photonics* **2018**, *12* (1), 9-17.
- (10) Jiang, Y.; Chen, Z.; Han, Y.; Deb, P.; Gao, H.; Xie, S.; Purohit, P.; Tate, M. W.; Park, J.; Gruner, S. M.; Elser, V.; Muller, D. A., Electron ptychography of 2D materials to deep sub-ångström resolution. *Nature* **2018**, *559* (7714), 343-349.
- (11) Odstrčil, M.; Menzel, A.; Guizar-Sicairos, M., Iterative least-squares solver for generalized maximum-likelihood ptychography. *Opt. Express* **2018**, *26* (3), 3108-3123.
- (12) Jiang, S.; Guo, C.; Song, P.; Zhou, N.; Bian, Z.; Zhu, J.; Wang, R.; Dong, P.; Zhang, Z.; Liao, J.; Yao, J.; Feng, B.; Murphy, M.; Zheng, G., Resolution-Enhanced Parallel Coded Ptychography for High-Throughput Optical Imaging. *ACS Photonics* **2021**, *8* (11), 3261-3271.
- (13) Jiang, S.; Guo, C.; Wang, T.; Liu, J.; Song, P.; Zhang, T.; Wang, R.; Feng, B.; Zheng, G., Blood-Coated Sensor for High-Throughput Ptychographic Cytometry on a Blu-ray Disc. *ACS Sensors* **2022**, *7* (4), 1058-1067.

- (14) Wang, T.; Jiang, S.; Song, P.; Wang, R.; Yang, L.; Zhang, T.; Zheng, G., Optical ptychography for biomedical imaging: recent progress and future directions [Invited]. *Biomed. Opt. Express* **2023**, *14* (2), 489-532.
- (15) Zheng, G.; Shen, C.; Jiang, S.; Song, P.; Yang, C., Concept, implementations and applications of Fourier ptychography. *Nature Reviews Physics* **2021**, *3* (3), 207-223.
- (16) Jiang, S.; Song, P.; Wang, T.; Yang, L.; Wang, R.; Guo, C.; Feng, B.; Maiden, A.; Zheng, G., Spatial- and Fourier-domain ptychography for high-throughput bio-imaging. *Nature Protocols* **2023**.
- (17) Brady, D. J.; Choi, K.; Marks, D. L.; Horisaki, R.; Lim, S., Compressive Holography. *Opt. Express* **2009**, *17* (15), 13040-13049.
- (18) Rivenson, Y.; Stern, A.; Javidi, B., Overview of compressive sensing techniques applied in holography [Invited]. *Applied Optics* **2013**, *52* (1), A423-A432.
- (19) Denis, L.; Lorenz, D.; Thiébaud, E.; Fournier, C.; Trede, D., Inline hologram reconstruction with sparsity constraints. *Opt. Lett.* **2009**, *34* (22), 3475-3477.
- (20) Shechtman, Y.; Beck, A.; Eldar, Y. C., GESPAR: Efficient phase retrieval of sparse signals. *IEEE transactions on signal processing* **2014**, *62* (4), 928-938.
- (21) Jaganathan, K.; Oymak, S.; Hassibi, B., Sparse phase retrieval: Uniqueness guarantees and recovery algorithms. *IEEE Transactions on Signal Processing* **2017**, *65* (9), 2402-2410.
- (22) Kostenko, A.; Batenburg, K. J.; Suhonen, H.; Offerman, S. E.; Van Vliet, L. J., Phase retrieval in inline x-ray phase contrast imaging based on total variation minimization. *Opt. Express* **2013**, *21* (1), 710-723.
- (23) Gaur, C.; Mohan, B.; Khare, K., Sparsity-assisted solution to the twin image problem in phase retrieval. *J. Opt. Soc. Am. A* **2015**, *32* (11), 1922-1927.
- (24) Zhang, W.; Cao, L.; Brady, D. J.; Zhang, H.; Cang, J.; Zhang, H.; Jin, G., Twin-Image-Free Holography: A Compressive Sensing Approach. *Physical Review Letters* **2018**, *121* (9), 093902.
- (25) Chang, H.; Lou, Y.; Duan, Y.; Marchesini, S., Total variation--based phase retrieval for Poisson noise removal. *SIAM journal on imaging sciences* **2018**, *11* (1), 24-55.
- (26) Guo, C.; Liu, X.; Kan, X.; Zhang, F.; Tan, J.; Liu, S.; Liu, Z., Lensfree on-chip microscopy based on dual-plane phase retrieval. *Opt. Express* **2019**, *27* (24), 35216-35229.
- (27) Gao, Y.; Yang, F.; Cao, L., Pixel Super-Resolution Phase Retrieval for Lensless On-Chip Microscopy via Accelerated Wirtinger Flow. *Cells* **2022**, *11* (13), 1999.
- (28) Yunhui, G.; Liangcai, C., Iterative projection meets sparsity regularization: towards practical single-shot quantitative phase imaging with in-line holography. *Light: Advanced Manufacturing* **2022**, *4* (1), 1-17.
- (29) Rivenson, Y.; Wu, Y.; Wang, H.; Zhang, Y.; Feizi, A.; Ozcan, A., Sparsity-based multi-height phase recovery in holographic microscopy. *Scientific Reports* **2016**, *6* (1), 37862.
- (30) Looock, S.; Plonka, G., Phase retrieval for Fresnel measurements using a shearlet sparsity constraint. *Inverse Problems* **2014**, *30* (5), 055005.
- (31) Pein, A.; Looock, S.; Plonka, G.; Salditt, T., Using sparsity information for iterative phase retrieval in x-ray propagation imaging. *Opt. Express* **2016**, *24* (8), 8332-8343.
- (32) Rudin, L. I.; Osher, S.; Fatemi, E., Nonlinear total variation based noise removal algorithms. *Physica D: nonlinear phenomena* **1992**, *60* (1-4), 259-268.
- (33) Chambolle, A., An Algorithm for Total Variation Minimization and Applications. *Journal of Mathematical Imaging and Vision* **2004**, *20* (1), 89-97.
- (34) Godard, P.; Allain, M.; Chamard, V.; Rodenburg, J., Noise models for low counting rate coherent diffraction imaging. *Opt. Express* **2012**, *20* (23), 25914-25934.
- (35) Maiden, A.; Johnson, D.; Li, P., Further improvements to the ptychographical iterative engine. *Optica* **2017**, *4* (7), 736-745.
- (36) Gao, Y.; Cao, L., A complex constrained total variation image denoising algorithm with application to phase retrieval. *arXiv preprint arXiv:2109.05496* **2021**.
- (37) Beck, A.; Teboulle, M., Fast Gradient-Based Algorithms for Constrained Total Variation Image Denoising and Deblurring Problems. *IEEE Transactions on Image Processing* **2009**, *18* (11), 2419-2434.

- (38) Dabov, K.; Foi, A.; Katkovnik, V.; Egiazarian, K., Image Denoising by Sparse 3-D Transform-Domain Collaborative Filtering. *IEEE Transactions on Image Processing* **2007**, *16* (8), 2080-2095.
- (39) Heide, F.; Diamond, S.; Nießner, M.; Ragan-Kelley, J.; Heidrich, W.; Wetzstein, G., Proximal: Efficient image optimization using proximal algorithms. *ACM Transactions on Graphics (TOG)* **2016**, *35* (4), 1-15.
- (40) Zhang, K.; Zuo, W.; Zhang, L., FFDNet: Toward a fast and flexible solution for CNN-based image denoising. *IEEE Transactions on Image Processing* **2018**, *27* (9), 4608-4622.
- (41) Lehtinen, J.; Munkberg, J.; Hasselgren, J.; Laine, S.; Karras, T.; Aittala, M.; Aila, T., Noise2Noise: Learning image restoration without clean data. *arXiv preprint arXiv:1803.04189* **2018**.
- (42) Huang, T.; Li, S.; Jia, X.; Lu, H.; Liu, J. In *Neighbor2neighbor: Self-supervised denoising from single noisy images*, Proceedings of the IEEE/CVF conference on computer vision and pattern recognition, 2021; pp 14781-14790.
- (43) Feng, B. T.; Smith, J.; Rubinstein, M.; Chang, H.; Bouman, K. L.; Freeman, W. T., Score-Based diffusion models as principled priors for inverse imaging. *arXiv preprint arXiv:2304.11751* **2023**.